

# Symmetry energy, unstable nuclei, and neutron star crusts

Kei Iida<sup>1,2</sup> and Kazuhiro Oyamatsu<sup>2,3</sup>

<sup>1</sup> Department of Natural Science, Kochi University, Akebono-cho, Kochi 780-8520, Japan

<sup>2</sup> RIKEN Nishina Center, Wako-shi, Saitama 351-0198, Japan

<sup>3</sup> Department of Human Informatics, Aichi Shukutoku University, 9 Katahira, Nagakute, Aichi 480-1197, Japan

Received: date / Revised version: date

**Abstract.** Phenomenological approach to inhomogeneous nuclear matter is useful to describe fundamental properties of atomic nuclei and neutron star crusts in terms of the equation of state of uniform nuclear matter. We review a series of researches that we have developed by following this approach. We start with more than 200 equations of state that are consistent with empirical masses and charge radii of stable nuclei and then apply them to describe matter radii and masses of unstable nuclei, proton elastic scattering and total reaction cross sections off unstable nuclei, and nuclei in neutron star crusts including nuclear pasta. We finally discuss the possibility of constraining the density dependence of the symmetry energy from experiments on unstable nuclei and even observations of quasi-periodic oscillations in giant flares of soft gamma-ray repeaters.

**PACS.** 21.65.Ef Symmetry energy – 21.10.Dr Binding energies and masses – 21.10.Gv Nucleon distributions and halo features – 24.50.+g Direct reactions – 26.60.Gj Neutron star crust – 97.10.Sj Pulsations, oscillations, and stellar seismology

## 1 Introduction

Determining the equation of state (EOS) of uniform nuclear matter is an old and fundamental issue in nuclear physics, but it is rather hard to solve [1]. Thus, it is still important to keep studying the EOS of nuclear matter phenomenologically and microscopically. Thanks to developments of neutron star observations and nuclear experiments, our interest in the EOS of nuclear matter has to extend for a very large region of density and neutron excess. In fact, nuclear matter associated with various systems, e.g., stable nuclei, unstable nuclei, nuclear pasta, neutron stars, supernova cores, heavy-ion collisions at intermediate energies, etc., has different density and neutron excess. On the other hand, our understanding is far from sufficient. Relatively well-known are pure neutron matter, which has been recently investigated from chiral effective theory interactions [2], and symmetric nuclear matter near normal nuclear density, which reflects the saturation of the nuclear binding energy and density. From there, theoretical extrapolations are more or less required. Moreover, one may still ask how large the saturation density of symmetric nuclear matter is within five percent errors. We remark that thermal effects are also important for supernova cores and heavy-ion collisions.

In describing the energy of uniform nuclear matter as function of density  $n$  and neutron excess  $\alpha = 1 - 2x$  with the proton fraction  $x$ , it is convenient to use an expansion of the energy per nucleon  $w$  around the saturation point

of symmetric nuclear matter [3],

$$w = w_0 + \frac{K_0}{18n_0^2}(n - n_0)^2 + \left[ S_0 + \frac{L}{3n_0}(n - n_0) \right] \alpha^2. \quad (1)$$

The parameters characterizing this expansion include the saturation density  $n_0$  and energy  $w_0$  of symmetric nuclear matter, the symmetry energy coefficient  $S_0$ , the incompressibility of symmetric nuclear matter  $K_0$ , and the density symmetry coefficient  $L$ . The parameters  $L$  and  $S_0$  are associated with the density dependent symmetry energy coefficient  $S(n)$  as  $S_0 = S(n_0)$  and  $L = 3n_0(dS/dn)_{n=n_0}$ . Basically, the parameter  $L$  corresponds to the pressure of pure neutron matter at  $n = n_0$ . Generally, higher order coefficients with respect to density such as  $K_0$  and  $L$  are more difficult to determine. We remark that expression (1) does not contain even higher order terms, one of which is associated with the isospin dependence of the incompressibility.

From the viewpoint of microscopic calculations, even pure neutron matter at low densities is not simple. This is because of strong coupling effects and uncertainties in the nuclear force. In fact, the Lee-Yang low density expansion only works at very low densities, while we can see a behavior close to the unitarity limit at densities where the scattering length is very large compared with interparticle spacing, which is in turn far larger than the range of the interaction [4]. Fortunately, in addition to variational calculations [5], elaborate Green's function Monte Carlo calculations [4] are available for pure neutron mat-

ter below normal nuclear density, and they are consistent with each other. More recently, systematic many-body calculations based on chiral effective field theory have been performed [2]. In these calculations, effects of three-body interactions play a role in determining the high density behavior of neutron matter EOS. On the other hand, symmetric nuclear matter is still more elusive. In fact, the saturation properties cannot be reproduced by variational calculations without a phenomenological three-body force [5]. This is partly due to complexity involving a strong tensor force.

In this article, we focus on a phenomenological approach to the EOS of nuclear matter. In sect. 2, a macroscopic nuclear model, which is constructed in such a way as to depend on the EOS of uniform nuclear matter, is reviewed. We show that  $L$  and  $K_0$  remain uncertain while empirical masses and charge radii of stable nuclei are equally well reproduced. The nuclear model is then used to describe matter radii and masses of unstable nuclei, proton elastic scattering and total reaction cross sections of unstable nuclei, and nuclei in neutron star crusts including nuclear pasta, which are given in sect. 3–6. In sect. 7, possible constraints on the density dependence of the symmetry energy from experiments on unstable nuclei and observations of quasi-periodic oscillations (QPOs) in giant flares of soft gamma-ray repeaters (SGRs) are discussed. Concluding remarks are finally given in sect. 8.

## 2 Macroscopic nuclear model

From now on, we will focus on a phenomenological approach to the EOS of nuclear matter. First we discuss the static properties of atomic nuclei and their relation with the EOS of nuclear matter on the basis of ref. [6]. To this end, we describe a macroscopic nuclear model in a manner that depends on the EOS of nuclear matter. Various applications can arise therefrom. For example, we will address in the next section how one can extract the saturation properties of asymmetric nuclear matter from the size of unstable nuclei. The main conclusion will be that it might be possible that we determine the density dependence of the symmetry energy from future systematic data for radii of unstable nuclei.

Application to neutron stars is of great significance because the EOS of nuclear matter at large neutron excess is relevant to the structure and evolution of neutron stars [7], which are expected to be further clarified by future space and ground-based observations. In the outer part (crust) of a star, nuclei present are considered to be very neutron rich or even drip neutrons in the presence of a neutralizing background of electrons. Near normal nuclear density, the system is considered to melt into uniform nuclear matter. This nuclear matter mainly constitutes the star's core and thus controls the structure of a neutron star.

The symmetry energy is related to the structure and evolution of neutron stars in many respects. For example, the mass and radius of a neutron star are mainly determined by the EOS of uniform nuclear matter. The symmetry energy acts to stiffen the EOS in a neutron-rich

situation as encountered in a star. Also, neutron star cooling is related to the symmetry energy since it controls the proton fraction in the core region. Fast neutrino emission process, i.e., direct URCA, can only occur at relatively high proton fraction.

Let us now start with the phenomenological expression for the energy of nuclear matter having the neutron and proton number densities  $n_n$  and  $n_p$ , which is divided into the kinetic energy part and the potential energy part as [8]

$$w = \frac{3\hbar^2(3\pi^2)^{2/3}}{10m_n n} (n_n^{5/3} + n_p^{5/3}) + (1 - \alpha^2) \frac{v_s(n)}{n} + \alpha^2 \frac{v_n(n)}{n}, \quad (2)$$

where

$$v_s = a_1 n^2 + \frac{a_2 n^3}{1 + a_3 n} \quad (3)$$

and

$$v_n = b_1 n^2 + \frac{b_2 n^3}{1 + b_3 n} \quad (4)$$

are the potential energy densities for symmetric nuclear matter and pure neutron matter, and  $m_n$  is the neutron mass (for simplicity we here identify the proton mass  $m_p$  with  $m_n$ ). The parameter  $b_3$ , which controls the EOS of matter for large neutron excess and high density and thus has little effect on the saturation properties of nearly symmetric nuclear matter, is set to  $1.58632 \text{ fm}^3$ , which was obtained by one of the authors [8] in such a way as to reproduce the neutron matter energy of Friedman and Pandharipande [5]. In the present energy expression, the potential energy part is a parabolic function of  $\alpha$ , while the kinetic energy part includes higher order terms in  $\alpha$ . Such  $\alpha$  dependence of the potential energy part is partially justified by variational calculations of Lagaris and Pandparihande [9].

Expression (2) is one of the simplest that reduces to the usual expression (1) near the saturation point of symmetric nuclear matter. From empirical masses and radii of stable nuclei, as we shall see, one can well determine the saturation density  $n_0$  and energy  $w_0$  of symmetric nuclear matter and the symmetry energy coefficient  $S_0$  [6]. The incompressibility  $K_0$  and the density symmetry coefficient  $L$  are relatively uncertain, but they control the saturation points at finite neutron excess. In fact, as the neutron excess increases from zero, the saturation point moves in the density versus energy plane. Up to second order in  $\alpha$ , the saturation energy  $w_s$  and density  $n_s$  are given by

$$w_s = w_0 + S_0 \alpha^2 \quad (5)$$

and

$$n_s = n_0 - \frac{3n_0 L}{K_0} \alpha^2. \quad (6)$$

The slope,  $y$ , of the saturation line near  $\alpha = 0$  ( $x = 1/2$ ) is thus expressed as

$$y = -\frac{K_0 S_0}{3n_0 L}. \quad (7)$$

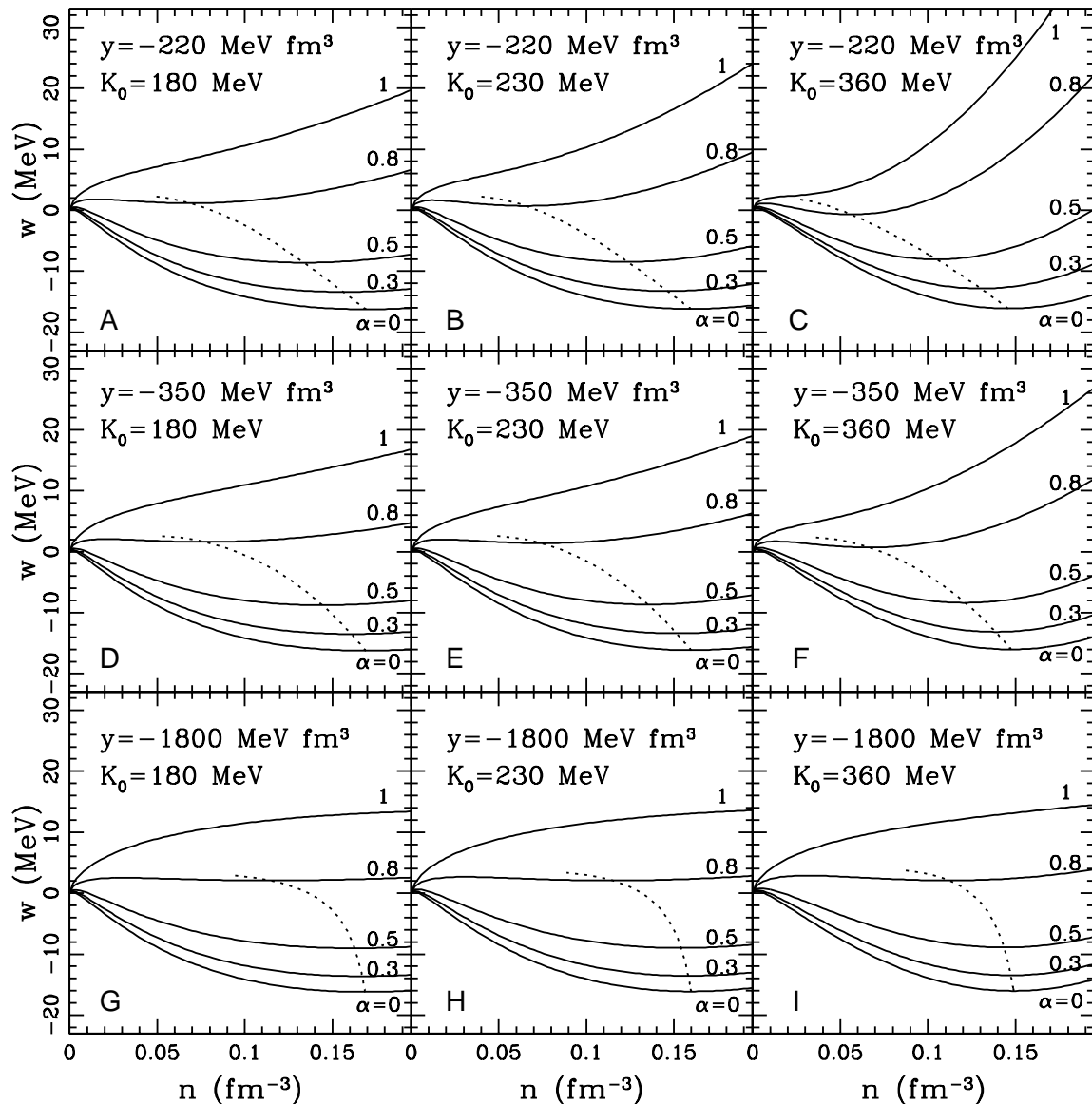


**Fig. 1.** Energy per nucleon of nuclear matter for nine extreme cases. In each panel, the solid lines are the energy at neutron excess  $\alpha = 0, 0.3, 0.5, 0.8, 1$ , and the dotted line is the saturation line. From ref. [10].

Figure 1 illustrates nine of the present EOS models, which can be obtained for various sets of the incompressibility  $K_0$  and the density symmetry coefficient  $L$  as will be shown below. In each panel we plot the energy as function of nucleon density ranging from symmetric nuclear matter to pure neutron matter. The saturation line is written in dashed line. As the incompressibility  $K_0$  increases, the curvature at the saturation point becomes larger. While, as the density symmetry coefficient  $L$  increases, the slope of the saturation line becomes gentler. The question of interest here is what kind of EOS is favored by empirical data on nuclear masses and radii.

For this purpose, we describe macroscopic nuclear properties in a way that is dependent on the EOS of nuclear matter by using a simplified version of the Thomas-Fermi model [6]. A similar approach was independently utilized by Bodmer and Usmani [11]. The essential point of the present model is to write down the binding energy of a nucleus of mass number  $A$  and charge number  $Z$  in a density functional form:

$$E = E_b + E_g + E_C + Nm_n c^2 + Zm_p c^2, \quad (8)$$

where

$$E_b = \int d^3r n(\mathbf{r}) w[n_n(\mathbf{r}), n_p(\mathbf{r})] \quad (9)$$

is the bulk energy,

$$E_g = F_0 \int d^3r |\nabla n(\mathbf{r})|^2 \quad (10)$$

is the gradient energy with adjustable constant  $F_0$ ,

$$E_C = \frac{e^2}{2} \int d^3r \int d^3r' \frac{n_p(\mathbf{r})n_p(\mathbf{r}')}{|\mathbf{r} - \mathbf{r}'|} \quad (11)$$

is the Coulomb energy, and  $N = A - Z$  is the neutron number. This form allows us to connect the EOS and the binding energy through the bulk energy part. For simplicity we use the following parametrization for the nucleon distributions ( $i = n, p$ ):

$$n_i(r) = \begin{cases} n_i^{\text{in}} \left[ 1 - \left( \frac{r}{R_i} \right)^{t_i} \right]^3, & r < R_i, \\ 0, & r \geq R_i. \end{cases} \quad (12)$$

Here,  $R_i$  roughly represents the nucleon radius,  $t_i$  the relative surface diffuseness, and  $n_i^{\text{in}}$  the central number density. The proton distribution of the form (12) can fairly accurately reproduce the empirical behavior from electron elastic scattering off stable nuclei.

In order to construct the nuclear model in such a way as to reproduce empirical masses and radii of stable nuclei, we first extremized the binding energy with respect to the particle distributions for fixed mass number  $A$ , five EOS parameters ( $n_0$ ,  $w_0$ ,  $K_0$ ,  $S_0$ , and  $L$ ), and gradient coefficient  $F_0$ . Next, for various sets of the incompressibility  $K_0$  and the density symmetry coefficient  $L$ , we obtained the remaining three EOS parameters as well as  $F_0$  by fitting the calculated optimal values of the nuclear charge number, mass, and root-mean-square (rms) charge radius to empirical data for stable nuclei on the smoothed beta stability line. Here we have defined the rms charge radius as

$$R_c = \left[ Z^{-1} \int d^3r r^2 \rho_c(\mathbf{r}) \right]^{1/2}, \quad (13)$$

where

$$\rho_c(\mathbf{r}) = (\pi^{1/2} a_p)^{-3} \int d^3r' \exp(-|\mathbf{r} - \mathbf{r}'|^2/a_p^2) n_p(\mathbf{r}') \quad (14)$$

with  $a_p = 0.65$  fm represents the charge distribution folded with the proton form factor [12]. The rms deviations of the calculated masses from the measured values [13] are of order 3 MeV, which are comparable with the deviations obtained from the Weizsäcker-Bethe mass formula, while the rms deviations of the calculated charge radii from the measured values [14] are about 0.06 fm, which are comparable with the deviations obtained from the  $A^{1/3}$  law.

In fig. 2 we exhibit the EOS parameter region that can be constrained from the fitting to empirical masses and radii of stable nuclei, together with various mean-field-model predictions. The saturation density  $n_0$  and energy  $w_0$  and the symmetry energy coefficient  $S_0$  are fairly well

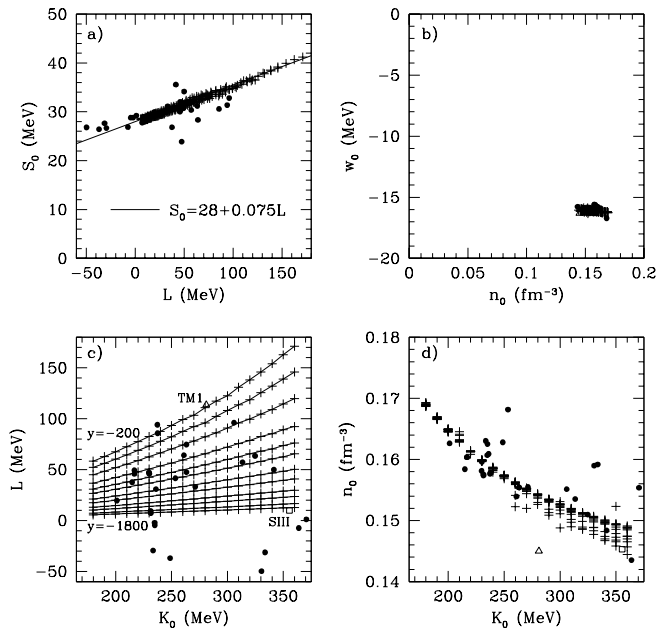


**Fig. 2.** Various optimal relations among the parameters  $S_0$ ,  $n_0$ ,  $w_0$ ,  $L$ , and  $K_0$  characterizing the EOS of nearly symmetric nuclear matter. In addition to the present results (crosses), the Skyrme-Hartree-Fock predictions [dots except for SIII (square)] and the TM1 prediction (triangle) are plotted. In (c), the thin lines are lines of constant  $y$ . From ref. [6].

constrained, while about 200 sets of the incompressibility  $K_0$  and the density symmetry coefficient  $L$  can provide reasonable fitting. In fact, the data fitting based on the least squares method depends on how to assign weights, which makes it impractical to find the optimal values of  $K_0$  and  $L$  among the sets, while for  $y$  higher than  $\sim -200$  MeV  $\text{fm}^3$ , the fitting becomes no longer effective. This  $K_0$ - $L$  region is a starting point of our study. We want to narrow this region by using future experiments for unstable nuclei. In the present analysis we rule out the possibility that the slope  $y$  is positive. A positive  $y$  is inconsistent with the fact that the empirical matter radii of  $A = 17, 20, 31$  isobars [15,16,17] tend to increase with neutron/proton excess. This is because a positive  $y$  plays a role in increasing the saturation density  $n_s$  with neutron/proton excess, as can be seen from eqs. (6) and (7).

It is also interesting to see the roughly linear relation between  $L$  and  $S_0$  in fig. 2. This tendency is not clear in the Skyrme-model calculations with zero-range force, but is known to be seen in the Gogny-model calculations with finite-range force [18]. How this tendency is related to the range of the three-nucleon force has been recently discussed [19]. We remark, however, that the roughly linear relation is consistent with a recent  $1\sigma$  fit to experimental masses and radii using a Skyrme-parametrized energy density functional [20].

The present  $L$ - $S_0$  relation can be compared with other constraints on  $L$  and  $S_0$ . It turns out that various constraints from heavy-ion data associated with isospin dif-

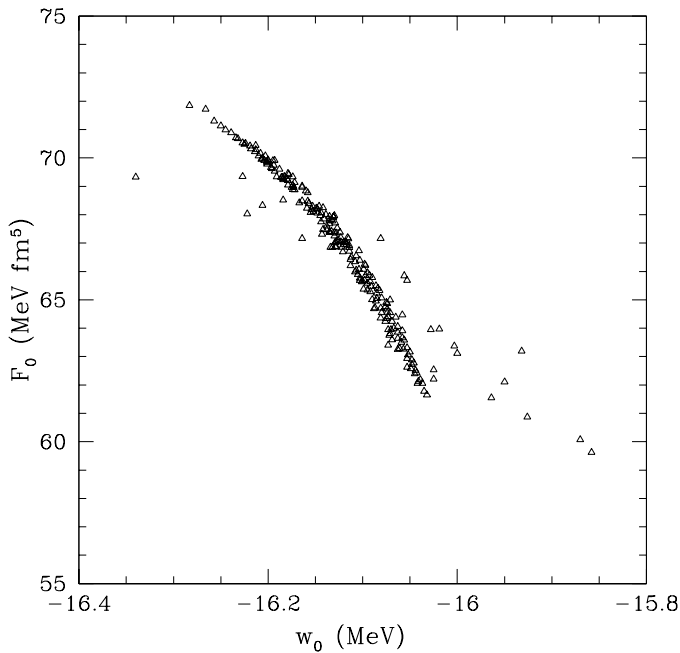


**Fig. 3.** Optimal relation of the gradient coefficient  $F_0$  with the saturation energy  $w_0$  of symmetric nuclear matter.

fusion and neutron-proton ratio, pigmy dipole resonances, excitation energies of isobaric analog states are not always consistent with each other [21]. Something has to be wrong, but we do not know which one. This may imply that data from stable nuclei are not enough to reasonably constrain  $L$ .

For completeness, in fig. 3 we exhibit the optimal values of  $F_0$ , which ranges  $\sim 60$ – $70$  MeV fm<sup>5</sup>, as a function of the optimal  $w_0$ . We note that there is a clear correlation between  $F_0$  and  $w_0$  because fitting to empirical masses requires a larger gradient energy for a larger bulk binding energy.

We conclude this section by summarizing salient features of the macroscopic nuclear model used here. This model can describe global nuclear properties such as masses and rms radii in a manner that is dependent on the EOS of nuclear matter, although it is not good at describing tails of the density distribution and does not allow for shell or pairing effects. As will be shown in the next section, the present macroscopic approach predicts that the matter radii depend appreciably on the density symmetry coefficient  $L$ , while being almost independent of the incompressibility  $K_0$ .

### 3 Matter radii of unstable nuclei

We now address how the EOS-dependent macroscopic nuclear model predicts the rms matter radii of unstable nuclei. As clarified in the previous section, the saturation density  $n_0$  and energy  $w_0$  and the symmetry energy coefficient  $S_0$  can be well determined from systematic data on

masses and radii of stable nuclei, while the incompressibility  $K_0$  and the density symmetry coefficient  $L$  are more difficult to determine. There are many trials of extracting the incompressibility from empirical data such as giant monopole resonances in stable nuclei [22] and even caloric curves in nuclear collisions [23]. Unfortunately this kind of extraction depends on models for the effective nucleon-nucleon interaction [24]. A decade ago, we proposed a method for extracting the density derivative of the symmetry energy from future systematic data on the matter radii of unstable nuclei on the basis of the macroscopic nuclear model [6]. In RIKEN and GSI, it is expected that RI beams of heavy nuclides incident on proton targets will provide elastic scattering data with reasonable accuracy, from which one may be able to deduce the matter radii, e.g., through an empirical relation between the first diffraction peak angles and the matter radii [25]. In GSI, this type of experiment named S272 was performed for <sup>70</sup>Ni several years ago, but the data remain unpublished.

Figure 4 shows the rms matter and charge radii for Ni and Sn isotopes calculated for various sets of  $K_0$  and  $L$ . Here we have defined the rms matter radius as

$$R_m = \left[ A^{-1} \int d^3r r^2 \rho_m(\mathbf{r}) \right]^{1/2}, \quad (15)$$

where

$$\rho_m(\mathbf{r}) = (\pi^{1/2} a_p)^{-3} \int d^3r' \exp(-|\mathbf{r} - \mathbf{r}'|^2/a_p^2) n(\mathbf{r}') \quad (16)$$

is the matter distribution folded with the proton charge form factor equally for neutrons and protons. At fixed  $K_0$ , differences of order 0.1 fm occur in the prediction of the matter radii of very neutron-rich nuclei due to uncertainties in the density symmetry coefficient  $L$ . This tendency arises because the saturation density at nonzero neutron excess decreases with increasing  $L$  as in eq. (6). On the other hand, the matter radii are almost independent of the incompressibility  $K_0$ . Note that as  $K_0$  increases, the surface diffuseness is reduced, while the saturation density  $n_0$  is also reduced as shown in fig. 2(d). We can thus conclude that these effects counteract with each other. Such  $K_0$  independence is promising for the purpose of deriving the value of  $L$  from the experimentally deduced matter radii. These are just plotted for stable nuclei by crosses, which are deduced from proton elastic scattering data by using optical potential models, but are not useful for derivation of  $L$ . Data for unstable nuclei are thus strongly desired.

It is often claimed that the neutron skin thickness of neutron-rich stable nuclei such as <sup>124</sup>Sn and <sup>208</sup>Pb can severely constrain  $L$  (e.g., ref. [27]). However, theoretical predictions of the neutron skin thickness depend not only on the nuclear bulk properties but also on the nuclear surface properties. In fact, within a compressible liquid-drop model [28, 29], one can show that the predicted neutron skin thickness, which is determined by a balance between the bulk and surface symmetry energies, has a linear dependence on  $L$ , but the poorly known density dependence of the surface tension prevents a model-independent constraint on  $L$ . Although the macroscopic nuclear model

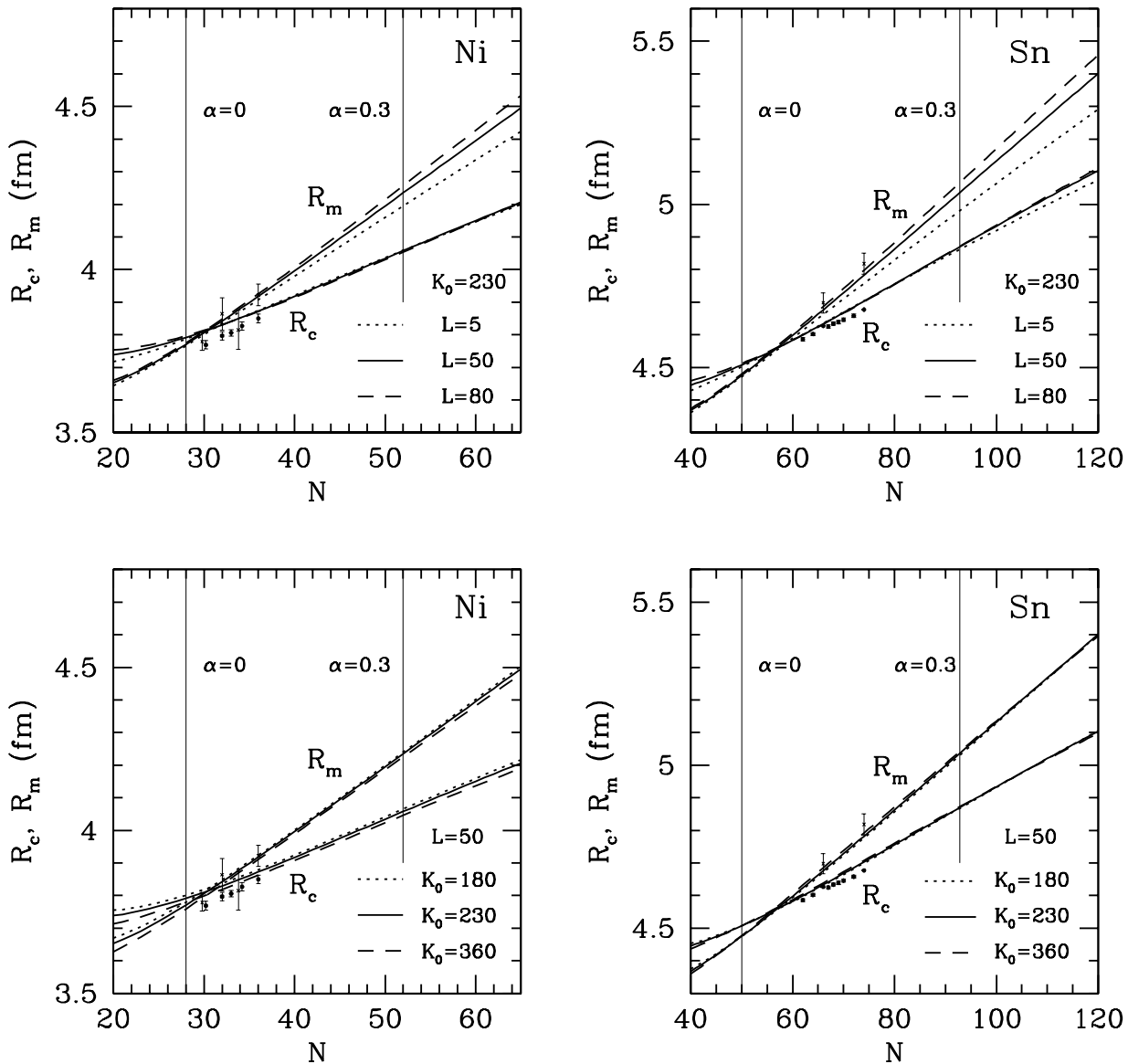


**Fig. 4.** The rms charge and matter radii,  $R_c$  and  $R_m$ , of Ni and Sn isotopes for combinations of  $L = 0, 50, 80$  MeV and  $K_0 = 180, 230, 360$  MeV. The experimental data for the rms charge radii (dots) and matter radii (crosses) are taken from refs. [14] and [26], respectively. From ref. [6].

used here and various mean-field models give a roughly linear correlation between  $L$  and the neutron skin thickness, respectively, such a correlation is significantly different between the two types of models. This kind of difference would affect a possible constraint on  $L$ . Note that the present macroscopic model tends to underestimate the surface diffuseness, which is not favorable for the prediction of the neutron skin thickness.

Several summarizing remarks on the contents in this and previous sections are in order. By using the macroscopic nuclear model, we derived the relations between the

EOS parameters from experimental data on the masses and charge radii of stable nuclei, and we found that  $L$  and  $K_0$  are still uncertain. The important prediction is that the density symmetry coefficient  $L$  may be determined if a global behavior of the matter radii at large neutron excess is obtained from future systematic measurements of the matter radii of unstable nuclei. Lastly, we remark that the parameter  $L$ , which characterizes the dependence of the EOS on neutron excess, is relevant to the structure and evolution of neutron stars through mass-radius relation, crust-core boundary, cooling, etc.

## 4 Proton elastic scattering and total reaction cross sections off unstable nuclei

It is not straightforward to deduce the matter radii of unstable nuclei from experimental data such as proton-nucleus elastic differential cross sections and total reaction cross sections because it requires the approximate scattering theory [26,30]. It is thus instructive to examine how the cross sections themselves are related to the parameter  $L$  in a proper theoretical framework, namely, the optical limit approximation of the Glauber multiple scattering model [31] that incorporates the nucleon distributions as obtained in sect. 2.

We first consider proton elastic scattering on the basis of ref. [32]. For sufficiently high proton incident energies and small momentum transfers to validate the Glauber model, we find that the angle of the scattering peak decreases with  $L$  more remarkably for larger neutron excess, while the peak height increases with  $K_0$  almost independently of neutron excess. We suggest the possibility that comparison of the calculations with experimental data for the peak angle may be useful for determination of  $L$ .

The elastic differential cross section at given momentum transfer  $\mathbf{q}$  and incident proton energy  $T_p$  can be written as (e.g., ref. [33])

$$\frac{d\sigma}{d\Omega} = |F(\mathbf{q})|^2, \quad (17)$$

with the elastic scattering amplitude,

$$|F(\mathbf{q})| = |F_C(\mathbf{q}) + \frac{ik}{2\pi} \int d\mathbf{b} e^{-i\mathbf{q}\cdot\mathbf{b} + 2i\eta \ln(k|\mathbf{b}|)} [1 - e^{i\chi_N(\mathbf{b})}]|. \quad (18)$$

Here,  $\hbar k = \sqrt{(T_p/c + m_p c)^2 - (m_p c)^2}$  is the incident proton momentum,  $\mathbf{b}$  is the impact parameter,  $\eta = Ze^2/\hbar v$  with the incident proton velocity  $v = \hbar k c / (T_p/c + m_p c)$  is the Sommerfeld parameter,

$$F_C(\mathbf{q}) = -\frac{2\eta k}{q^2} \exp \left[ -2i\eta \ln \left( \frac{|\mathbf{q}|}{2k} \right) + 2i \arg \Gamma(1 + i\eta) \right] \quad (19)$$

is the amplitude of the Coulomb elastic scattering, which we approximate as a usual Rutherford scattering off a point charge, and

$$i\chi_N(\mathbf{b}) = - \int d\mathbf{r} [n_p(\mathbf{r}) \Gamma_{pp}(\mathbf{b}-\mathbf{s}) + n_n(\mathbf{r}) \Gamma_{pn}(\mathbf{b}-\mathbf{s})] \quad (20)$$

is the phase shift function with the projection  $\mathbf{s}$  of the coordinate  $\mathbf{r}$  on a plane perpendicular to the incident proton momentum and with the profile function  $\Gamma_{pN}$  of the free proton-nucleon ( $pN$ ) scattering amplitude, for which we use a simple parametrization,

$$\Gamma_{pN}(\mathbf{b}) = \frac{1 - i\alpha_{pN}}{4\pi\beta_{pN}} \sigma_{pN} \exp(-\mathbf{b}^2/2\beta_{pN}), \quad (21)$$

where  $\alpha_{pN} = -\text{Im}\Gamma_{pN}(0)/\text{Re}\Gamma_{pN}(0)$ ,  $\sigma_{pN}$  is the  $pN$  total cross section, and  $\beta_{pN}$  is the slope parameter. Here

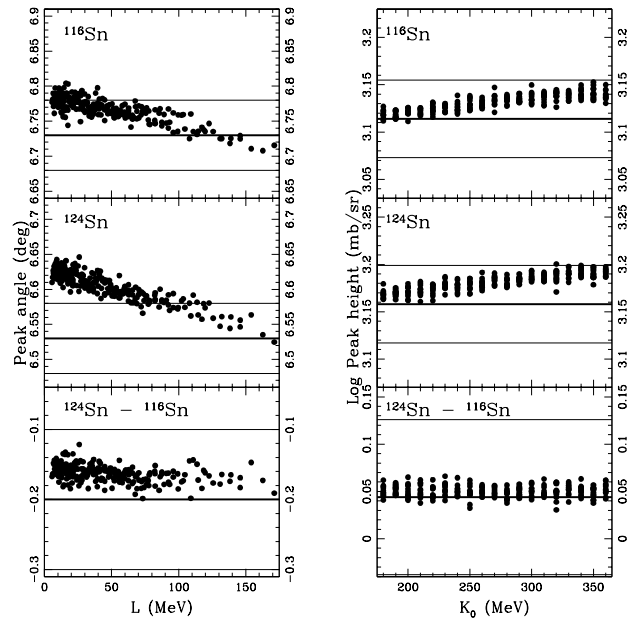


**Fig. 5.** The angles and heights of the scattering peak in the small angle regime, calculated as functions of  $L$  and  $K_0$  for  $p$ - $^{116}\text{Sn}$  and  $p$ - $^{124}\text{Sn}$  elastic scattering at  $T_p = 800$  MeV. The experimental angles and heights including errors (from ref. [35]) are denoted by the horizontal lines (thick lines: central values, thin lines: upper and lower bounds). From ref. [32].

the values of  $\alpha_{pN}$ ,  $\beta_{pN}$ , and  $\sigma_{pN}$  at given incident proton energy  $T_p$  are taken from ref. [34].

Generally, the peak angles are related to the nuclear size, while the peak heights are related to the surface diffuseness. In our macroscopic calculations, the radius and diffuseness are in turn related to the EOS parameters. For larger density symmetry coefficient  $L$  we obtain a larger radius, while for larger incompressibility  $K_0$  we obtain a smaller surface diffuseness. So it is interesting to investigate the detailed peak structure in the small angle regime and its relation with the EOS parameters.

In fig. 5 we illustrate the scattering angles and heights in the first peak, calculated for about 200 sets of the EOS parameters in the case of stable Sn isotopes at incident energy of 800 MeV. The peak angle decreases with  $L$ . This is an important property which might enable us to extract  $L$  from comparison with the experimental peak angle. However, such extract is difficult in this case because the experimental uncertainty due to the absolute angle calibration, which is taken to be 0.05 deg, is too large to distinguish between different  $L$ 's for nuclei having neutron excess of order or smaller than 0.2.

On the other hand, the peak height increases with the incompressibility  $K_0$  in a way almost independent of neutron excess. However, it is also difficult to extract  $K_0$  from comparison with the experimental peak height mainly because our semi-classical nuclear model tends to underestimate the surface diffuseness.

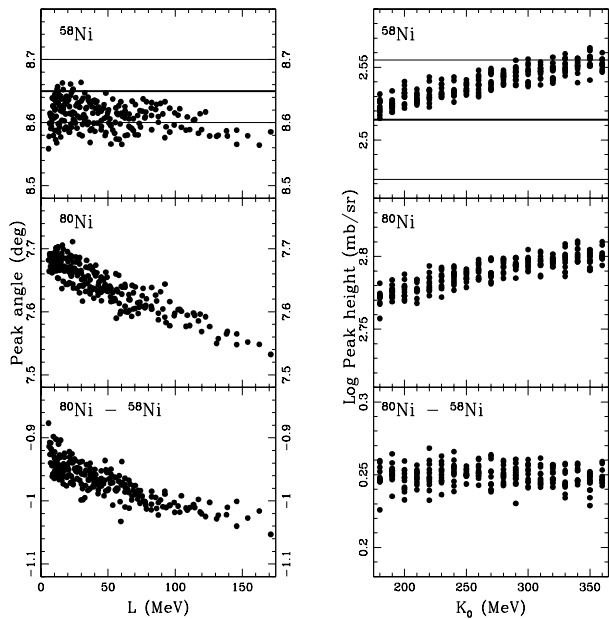


**Fig. 6.** Same as fig. 5 for  $p$ - $^{58}\text{Ni}$  and  $p$ - $^{80}\text{Ni}$  elastic scattering at  $T_p = 800$  MeV. From ref. [32].

We move on to scattering off unstable nuclei, whose beams incident on proton targets can provide elastic scattering data. Here we consider a very neutron-rich nucleus  $^{80}\text{Ni}$ . In fact, the neutron excess for  $^{80}\text{Ni}$  amounts to 0.3. We perform the calculations for  $^{58}\text{Ni}$  and  $^{80}\text{Ni}$  at incident energy of 800 MeV. We find from fig. 6 that the  $L$  dependence of the difference in the peak angle between the  $^{58}\text{Ni}$  and  $^{80}\text{Ni}$  cases looks large enough to enable us to extract  $L$ . It is now useful to take the difference because our calculations based on the macroscopic nuclear model contain systematic errors by ignoring pairing and shell effects and tails of the nucleon distributions. In order to take full care of such systematic errors, systematic measurements of the peak angles in the small angle region for various nuclides are desired for as large neutron excess as possible with accuracy of order 0.01 deg. According to the usual Fraunhofer diffraction, the difference of order 0.01 deg in the peak angle corresponds to the difference of order 0.01 fm in the rms matter radius. We remark in passing that the present analysis eventually developed into a black sphere model [25] that gives a nuclear length scale that characterizes measured total reaction cross sections and elastic diffraction peak angles simultaneously.

We finally consider proton-nucleus total reaction cross sections, which can be calculated from the same Glauber model as used for the elastic scattering calculations [36]. The total reaction cross section can be written as

$$\sigma_R = \int d\mathbf{b} \left( 1 - \left| e^{i\chi_N(\mathbf{b})} \right|^2 \right), \quad (22)$$

where  $\chi_N$  is given by eq. (20).

Figure 7 shows the results for the selected isotopes at  $T_p = 800$  MeV. The dependence of the total reaction cross

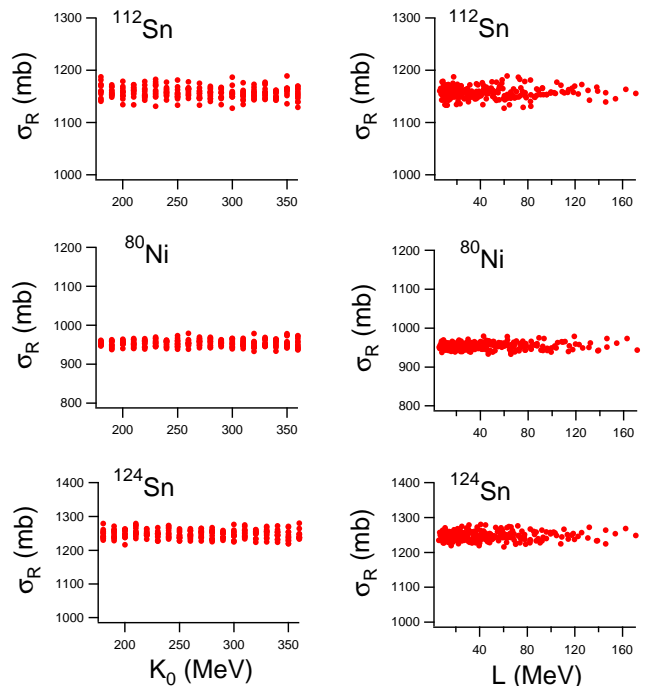


**Fig. 7.** (Color online) The total reaction cross sections calculated as a function of  $K_0$  and  $L$  for  $p$ - $^{112,124}\text{Sn}$  and  $p$ - $^{80}\text{Ni}$  at  $T_p = 800$  MeV. From ref. [36].

section  $\sigma_R$  on the EOS parameters is weak even for very neutron-rich nuclei such as  $^{80}\text{Ni}$ , in contrast to the case of elastic scattering in which a strong  $L$  (or size) dependence of the calculated diffraction peak angle appears for  $^{80}\text{Ni}$  as shown in fig. 6. This was not expected from a standard picture that the larger size, the larger  $\sigma_R$ , but in fact reflects a feature of the optical limit Glauber theory in which an unphysical exponential dependence of the reaction cross section on the neutron skin thickness remains when the total proton-neutron cross section is small enough [36]. For duly describing the size dependence of the total reaction cross sections, therefore, alternative approaches based on empirical data for the total reaction cross sections such as those in refs. [37] and [38] might be useful even for high incident energies where the Glauber theory is usually assumed to be valid.

We remark that differences between interaction cross sections and total reaction cross sections are often ignored, which causes interaction cross sections, whose data are far easier to obtain experimentally, to be identified with total reaction cross sections. However, this is not always the case even for high energy data, as suggested by using pseudodata for total reaction cross sections that can be obtained from the measured elastic diffraction peak angles for stable nuclei via the black sphere model [39]. Within the framework of the full Glauber scattering theory, Novikov and Shabelski [40] also confirmed that the differences are appreciable.



## 5 Nuclear masses of unstable nuclei

Let us move on to nuclear masses. The mass has an advantage over the size because empirical mass data have been already accumulated for unstable nuclei. Then, it is natural to ask if the existing data for masses of unstable nuclei is useful for determination of  $L$ . We shall give a tentative answer on the basis of refs. [41,42].

We want to know the global neutron excess dependence of nuclear masses. To this end, some kind of differentials are useful. Here we focus on the two proton separation energy  $S_{2p}(Z, N) = E_B(Z, N) - E_B(Z - 2, N)$  with the nuclear binding energy  $E_B$ . As illustrated in ref. [43], for fixed proton number  $Z$ , the empirical values of  $S_{2p}$  and also the values from the Koura-Tachibana-Uno-Yamada (KTUY) mass formula show a very smooth isospin dependence except for proton shell gaps. Moreover, the even-odd staggering essentially disappears in the two proton separation energy  $S_{2p}$ . On the other hand, the two neutron separation energy  $S_{2n} = E_B(Z, N) - E_B(Z, N - 2)$  does not show an ideal isospin dependence at fixed  $Z$ , because it has a very large discontinuity around neutron magic numbers.

We now try to compare the empirical  $S_{2p}$  and the predictions from the EOS models C and G shown in fig. 1 by using the macroscopic nuclear model. As exhibited in fig. 8, the empirical  $S_{2p}$  shows a smooth dependence on neutron excess except for symmetric nuclei, nuclei with neutron magic numbers, and deformed nuclei. On the other hand, the calculated  $S_{2p}$  shows a larger neutron excess dependence for larger  $L$ . Comparison between the empirical and calculated  $S_{2p}$  seems easier for smaller mass. As far as the slope of  $S_{2p}$  with respect to neutron excess is concerned, a larger  $L$  value is more consistent with the empirical data. Note that there are roughly uniform offsets between the data and the calculations with the EOS model C at  $N > Z$ , which are presumably due to proton shell gaps ignored in the present calculations. That is why the fact that the calculated  $S_{2p}$  from the EOS model G is apparently closer to the empirical  $S_{2p}$  has to be seen with caution.

In order to understand the  $L$  dependence of  $S_{2p}$ , we go back to the  $L$  dependence of the calculated nuclear masses. For very neutron rich nuclei, as shown in fig. 9, the calculated mass decreases with  $L$ , while having a relatively weak dependence on  $K_0$ . This suggests that nuclear masses are not always dominated by the bulk properties of nuclear matter. In fact, the  $L$  dependence of the calculated mass cannot be explained by the bulk asymmetry term because for a larger  $L$  we obtain a larger  $S_0$  (see fig. 2), leading to a larger mass according to eq. (5). Therefore, we can conclude that the surface asymmetry term is responsible for the present  $L$  dependence of the calculated mass. In fact, within a compressible liquid-drop model [28,29], one can show that the surface tension for neutron rich nuclei is effectively smaller for larger  $L$ , leading to a smaller mass and  $S_{2p}$ .

Note that the macroscopic nuclear model used here effectively has a nonvanishing density dependence of the surface tension. This is a contrast to the cases of many

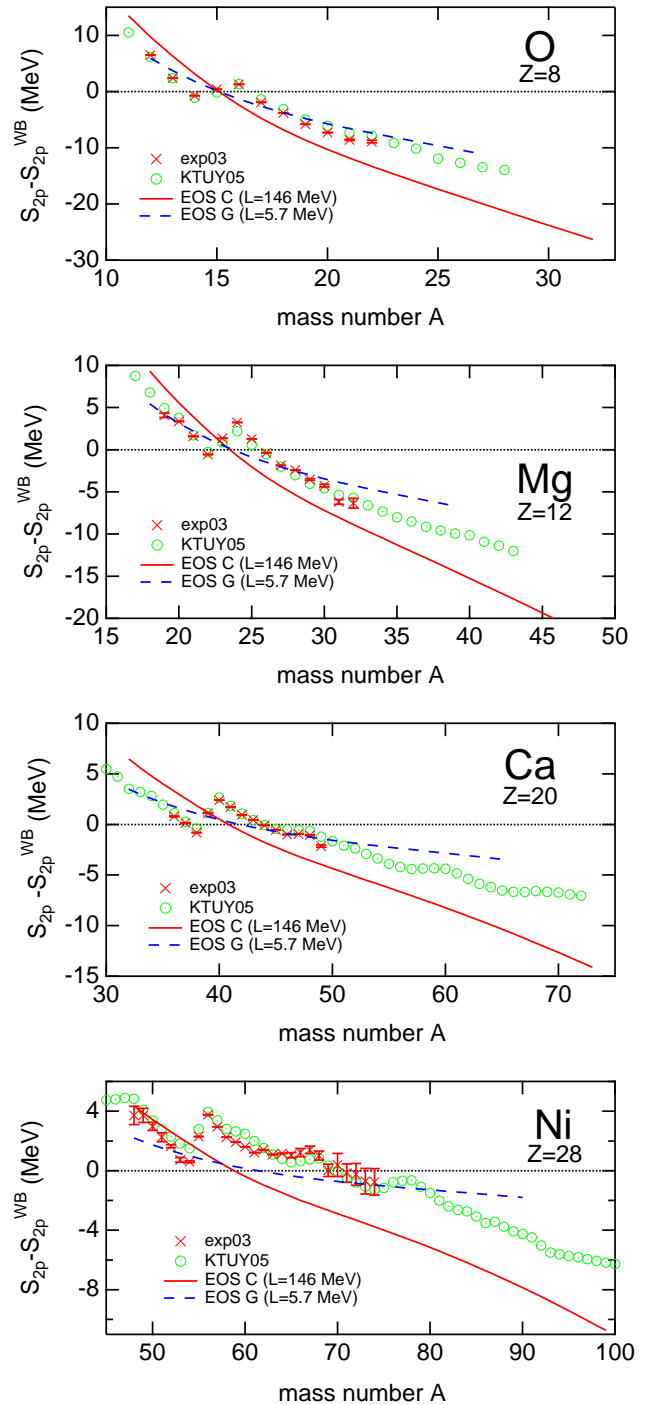


**Fig. 8.** (Color online) The two-proton separation energy, having the one calculated from a Weizsäcker-Bethe mass formula [28] subtracted out, for O, Mg, Ca, and Ni isotopes. The empirical values [13], the calculated values from the EOS models C and G, and the values obtained from a contemporary mass formula [43] are plotted in each panel. From ref. [41].

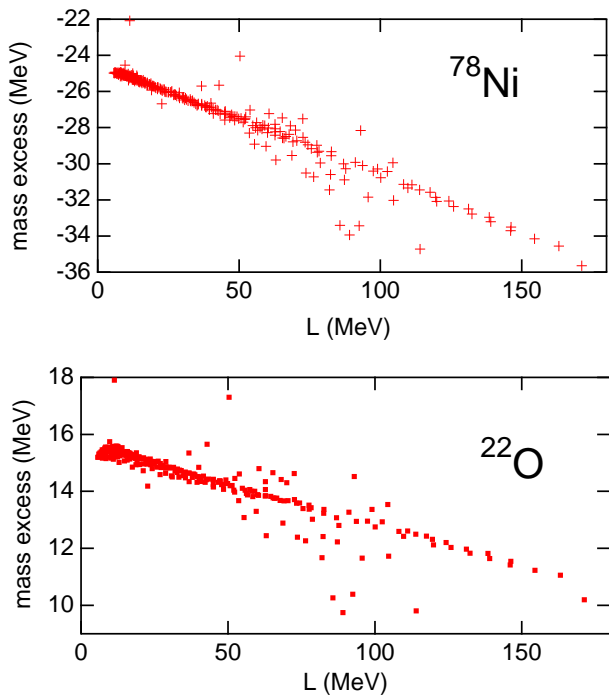


**Fig. 9.** (Color online) The mass excess calculated for  $^{78}\text{Ni}$  and  $^{22}\text{O}$  as a function of  $L$ . From ref. [41].

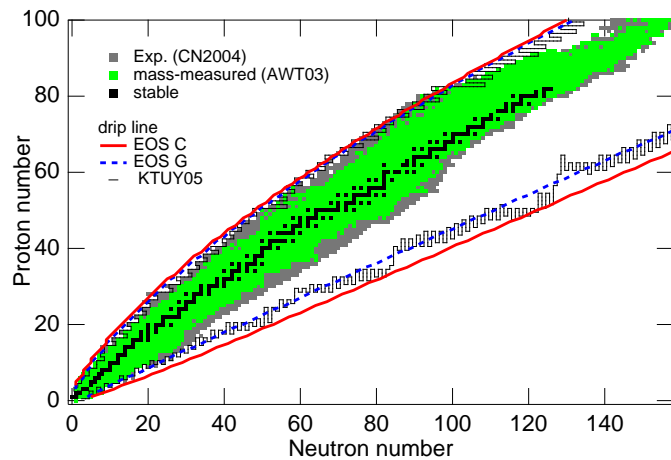


**Fig. 10.** (Color online) The neutron and proton drip lines obtained from the EOS models C and G by using the macroscopic nuclear model and from a contemporary mass formula [43]. The regions filled with squares correspond to empirically known nuclides [44, 45]. From ref. [42].

compressible liquid-drop models that assume vanishing density dependence of the surface tension. However, this assumption applies only for the planar interface between the bulk liquid and gas (vacuum) phases where under mechanical stability, the nucleon density is fixed at the saturation density and zero, respectively. A possible constraint on  $L$  from empirical nuclear masses would thus depend on the adopted density dependence of the surface tension. This situation is similar to the case of the neutron skin thickness.

As an important application, we proceed to exhibit the neutron drip line, which was calculated from the EOS models C and G within the macroscopic nuclear model and from the KTUY mass formula [42]. In fig. 10, the neutron drip line was drawn by identifying nuclides at neutron drip with those neighboring to nuclides for which  $S_n = E_B(Z, N) - E_B(Z, N - 1)$  and  $S_{2n}$  are positive and beyond which at least one of them is negative. As  $L$  increases, the calculated drip line shifts to the neutron rich side on the chart of nuclides, because for larger  $L$  we obtain more binding through the surface properties discussed above. Consequently, this shift is appreciable for small masses where some of the drip nuclei are empirically identified [46, 47]. It is an interesting open question to constrain  $L$  from the empirical drip line to be expanded in the near future. Note, however, that the neutron drip line is mainly determined by a competition between the Coulomb energy and the symmetry energy coefficient  $S_0$ , while the present  $L$  effect, induced by the surface properties, is just secondary.

## 6 Nuclei in neutron star crusts and nuclear pasta

Let us turn to a different topic of research, namely, neutron star crusts. On the basis of ref. [10], we will show that the presence of nuclear pasta in neutron stars is sensitive to the density symmetry coefficient  $L$ .

Nuclear pasta represents exotic shapes of nuclei, which may occur in the deepest region of the crust [48, 49]. In this region, nuclei are considered to be closely packed in a bcc Coulomb lattice. Then, the total surface area becomes very large. In order to lower the system energy, it is convenient that the spherical nuclei are elongated and fuse into a nuclear rod. In the presence of Coulomb energy, the nuclei cannot have arbitrary shape. With the density increased further, possible changes in nuclear shape are considered to be rods, slabs, tubes, bubbles, and uniform. In terms of liquid crystals, the rod and tube phases are columnar, while the slab phase is smectic A. Also these pasta phases can be regarded as liquid-gas mixed phases. As we will see, the symmetry energy at subnuclear densities controls the crust-core boundary and the presence of nuclear pasta.

In describing zero-temperature matter in neutron star crusts, we again use the macroscopic nuclear model. This time, not for a nucleus in vacuum, but for a nucleus or bubble in a Wigner-Seitz cell. New additions are dripped neutrons, a neutralizing uniform background of electrons, and the lattice energy.

For each unit cell, we write the total energy as

$$W = W_N + W_e + W_C, \quad (23)$$

where  $W_N$ ,  $W_e$ , and  $W_C$  are the nuclear energy, the electron energy, and the Coulomb energy.

As in eq. (8), the nuclear energy is again expressed in the density functional form:

$$W_N = \int_{\text{cell}} d^3r \{n(\mathbf{r})w[n_n(\mathbf{r}), n_p(\mathbf{r})] + m_n c^2 n_n(\mathbf{r}) + m_p c^2 n_p(\mathbf{r}) + F_0 |\nabla n(\mathbf{r})|^2\}. \quad (24)$$

For a spherical nucleus in vacuum, this expression reduces to  $E - E_C$  [see eq. (8)].

The electron energy can be approximated as the energy of an ideal uniform Fermi gas,

$$\frac{W_e}{a^3} = \frac{m_e^4 c^5}{8\pi^2 \hbar^3} \{x_e(2x_e^2 + 1)(x_e^2 + 1)^{1/2} - \ln[x_e + (x_e^2 + 1)^{1/2}]\} \quad (25)$$

with

$$x_e = \frac{\hbar(3\pi^2 n_e)^{1/3}}{m_e c}, \quad (26)$$

where  $m_e$  is the electron mass, and  $n_e$  is the electron number density that satisfies the charge neutrality condition,

$$a^3 n_e = \int_{\text{cell}} d^3r n_p(\mathbf{r}). \quad (27)$$

We remark that  $n_e$  is so high that we can safely ignore inhomogeneity of the electron density induced by the electron screening of nuclei or bubbles and the Hartree-Fock corrections to the electron energy.

The Coulomb energy, which is composed of the proton self-Coulomb energy and the lattice energy, can be written as

$$W_C = \frac{1}{2} \int_{\text{cell}} d^3r e[n_p(\mathbf{r}) - n_e]\phi(\mathbf{r}) + \Delta W_1, \quad (28)$$

where  $\phi(\mathbf{r})$  is the electrostatic potential in a Wigner-Seitz cell, and  $\Delta W_1$  is the difference of the rigorous calculation [50] for a cell in the bcc (triangular) lattice of spherical (cylindrical) nuclei or bubbles having sharp surfaces from the Wigner-Seitz value, as parametrized in ref. [8]. We take into account  $\Delta W_1$ , which is a less than 1 % correction, because  $\Delta W_1$  depends sensitively on the dimensionality of the lattice.

For nucleon distributions in the Wigner-Seitz cell, we simply generalize the parametrization (12) for a nucleus in vacuum into

$$n_i(r) = \begin{cases} (n_i^{\text{in}} - n_i^{\text{out}}) \left[1 - \left(\frac{r}{R_i}\right)^{t_i}\right]^3 + n_i^{\text{out}}, & r < R_i, \\ n_i^{\text{out}}, & R_i \leq r. \end{cases} \quad (29)$$

Here  $r$  is the distance from the central point, axis, or plane of the unit cell. In the case of nuclei,  $n_p^{\text{out}} = 0$ , while in the case of bubbles,  $n_p^{\text{in}} = 0$ .

We finally determine the equilibrium configuration of the system at given baryon density,

$$n_b = a^{-3} \int_{\text{cell}} d^3r n(\mathbf{r}). \quad (30)$$

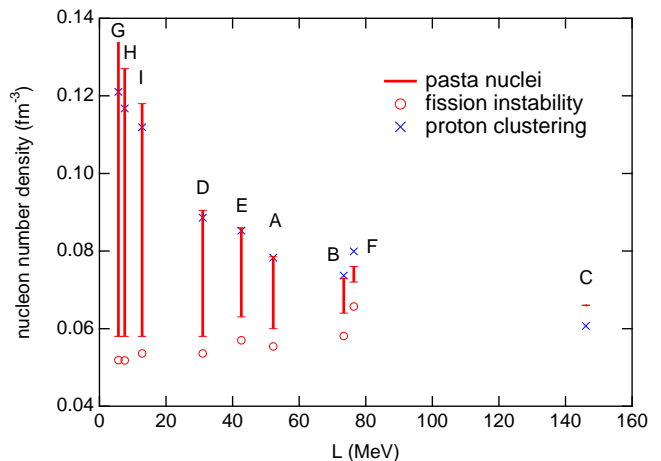


**Fig. 11.** (Color online) The density region containing bubbles and nonspherical nuclei as a function of  $L$ , calculated for the EOS models A–I in fig. 1. For comparison, the density corresponding to  $u = 1/8$  in the phase with spherical nuclei and the onset density of proton clustering in uniform nuclear matter are also plotted by circles and crosses, respectively. From ref. [10].

First, for each of the five inhomogeneous phases, we minimize the total energy density  $W/a^3$  with respect to the eight parameters  $a$ ,  $n_n^{\text{in}}$ ,  $n_n^{\text{out}}$ ,  $n_p^{\text{in}}$  (for nuclei) or  $n_p^{\text{out}}$  (for bubbles),  $R_n$ ,  $R_p$ ,  $t_n$ , and  $t_p$ . This minimization implicitly allows for the stability of the nuclear matter region (the region containing protons) with respect to change in the size, neutron drip,  $\beta$ -decay, and pressurization. In addition to the five inhomogeneous phases, we consider a uniform phase of  $\beta$ -equilibrated, neutral nuclear matter. The energy density of this phase is the sum of the nucleon part  $nw + m_n c^2 n_n + m_p c^2 n_p$  [see eq. (2)] and the electron part (25). By comparing the resultant six energy densities, we can determine the equilibrium phase of energy density  $\rho$ .

In fig. 11, we show the resultant density region where pasta nuclei are predicted to appear. We find that the larger  $L$ , the narrower pasta region. This tendency suggests that for smaller symmetry energy at subnuclear densities, protons become more difficult to cluster in uniform matter.

The lower end of the pasta region can be naively understood from fissionlike instability of spherical nuclei. In a liquid-drop model, it is predicted that nuclei tend toward quadrupolar deformations when the Coulomb energy is twice as large as the surface energy. In neutron stars, due to the lattice energy, this condition can be essentially met even in equilibrium when the volume fraction of nuclei reaches  $1/8$ . At this volume fraction, the baryon density is of order  $0.06 \text{ fm}^{-3}$  and almost independent of the EOS models, as shown in fig. 12.

On the other hand, the upper end of the pasta region can be naively understood from proton clustering instability of uniform matter. The tendency to proton clustering can be measured by the sign change of the effective potential between proton density fluctuations. The driving force of proton clustering is the symmetry energy at sub-

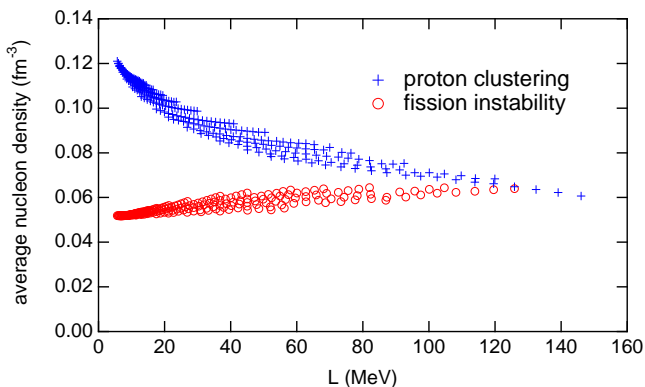


**Fig. 12.** (Color online) The onset density of proton clustering in uniform nuclear matter calculated from the present EOS models. For comparison, we plot the density corresponding to  $u = 1/8$  in the phase with spherical nuclei. From ref. [10].

nuclear densities. In fact, for larger  $L$ , the system keeps homogeneous down to lower density, as shown in fig. 12.

Comparing the onset densities of proton clustering and fission instability with the equilibrium calculations of the pasta region, we find that the onset densities are a good measure of the pasta region (see fig. 11). Judging from fig. 12, the critical value of  $L$  for the presence of pasta nuclei in neutron stars is about 100 MeV.

Recently, more complicated structures with intersecting rods have been predicted by calculations beyond the Wigner-Seitz approximation [51, 52, 53, 54, 55, 56]. On the other hand, a liquid-drop approach [57, 58] can be used for the purpose of examining the possible occurrence of a periodic bicontinuous structure, namely, gyroid, which is known to occur in polymer systems [59]. Energetically, this structure is to be reckoned with seriously judging from the evaluated energy difference from the ground state at subnuclear densities, but even with shape-dependent curvature effects included, no density region where the gyroid is most stable was found.

At finite temperatures, pasta nuclei do not always have perfect structure. In fact, they thermally fluctuate just like molecular liquid crystals. At typical temperatures of neutron star interiors, however, the amplitude of the displacements involved is smaller than internuclear spacing [60].

We conclude this section by showing the size of spherical nuclei in the inner crust estimated for various EOS models within the macroscopic nuclear model. We find from fig. 13 that the larger  $L$ , the smaller size. This tendency suggests that for larger  $L$  or, equivalently, smaller symmetry energy at subnuclear density, the density of dripped neutrons becomes larger and hence the surface tension becomes smaller. This is essential to possible constraints on  $L$  from neutron star asteroseismology as will be discussed in the next section.

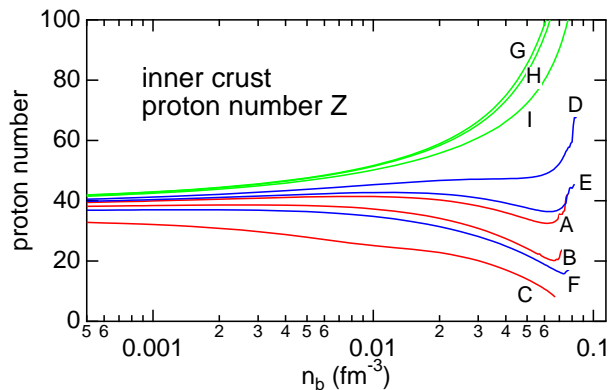


**Fig. 13.** (Color online) The charge number of spherical nuclei as a function of  $n_b$ , calculated for the EOS models A–I. From ref. [10].

## 7 Possible constraints on $L$

In this section we consider possible constraints on  $L$  from empirical data via the macroscopic nuclear model. As discussed in sect. 5, experimental data on masses of unstable nuclei could give a stringent constraint on  $L$  if the model were free from systematic errors associated with the description of the isospin-dependent surface properties. In fact, constraints on  $L$  that were obtained from the mass data in earlier publications scatter [61]. All we can conclude at this stage is that a very small  $L$  cannot reproduce the empirical isotope dependence of the two-proton separation energy  $S_{2p}$  depicted in fig. 8. On the other hand, future systematic data associated with the size of unstable nuclei are expected to help constrain  $L$  as discussed in Secs. 3 and 4.

We finally turn to QPOs in giant flares from SGRs and their possible relation with crustal torsional oscillations. Usually, SGRs are considered to be magnetars, i.e., neutron stars with surface magnetic fields of order  $10^{15}$  G. About a decade ago, one of them exhibited a giant flare and fortunately, its X-ray afterglow was detected by the Rossi X-ray Timing Explorer [62]. It turns out that the afterglow oscillates quasi-periodically.

Steiner and Watts [63] tried to explain these QPOs in terms of crustal shear modes. They succeeded in reproducing some of the measured frequencies, but the analysis is model dependent. This is because the shear modulus is controlled by the charge number of neutron-rich nuclei that constitute the crust, and the charge number is predicted to be dependent on  $L$  as shown in fig. 13.

With this  $L$  dependence of the charge number in mind, we evaluated the frequency of the fundamental mode of crustal torsional oscillation by ignoring and allowing for the effects of neutron superfluidity [64, 65]. For such evaluations, we first consider the equilibrium neutron star configurations. Since the magnetic energy is much smaller than the gravitational binding energy even for magnetars, we can neglect the deformation due to the magnetic pressure. Additionally, since the magnetars are relatively slowly rotating, we can also neglect the rotational

effect. Hereafter, therefore, we consider spherically symmetric neutron stars, whose structure is described by the solutions of the well-known Tolman-Oppenheimer-Volkoff (TOV) equations. In this case, the metric can be expressed in terms of the spherical polar coordinates  $r$ ,  $\theta$ , and  $\phi$  as

$$ds^2 = -e^{2\Phi} dt^2 + e^{2\Lambda} dr^2 + r^2 d\theta^2 + r^2 \sin^2 \theta d\phi^2, \quad (31)$$

where  $\Phi$  and  $\Lambda$  are functions of  $r$ . (Hereafter, we use units in which  $G = c = 1$ .) We remark that  $\Lambda(r)$  is associated with the mass function

$$m(r) = \int_0^r dr' 4\pi r'^2 \rho(r') \quad (32)$$

as  $e^{2\Lambda} = [1 - 2m(r)/r]^{-1}$ .

To solve the TOV equations, one generally uses the zero-temperature EOS, i.e., the pressure  $p$  as a function of the mass density  $\rho$ . For matter in the crust, we use the same EOS models as described above. Unfortunately, the core EOS is still uncertain in the absence of clear understanding of the constituents and their interactions both in vacuum and in medium. Since we will focus on shear torsional oscillations that occur in the crust, we can effectively describe such uncertainties in the core EOS by solely setting the star's mass  $M$  and radius  $R$  as free parameters, without using specific models for the core EOS. In fact, for various sets of  $M$  and  $R$ , we systematically construct the equilibrium configuration of the crust by integrating the TOV equations with the crust EOS from the star's surface all the way down to the crust-core boundary. This is a contrast to the usual way of constructing a star by initially giving a value of the central mass density and then integrating the TOV equations with a specific model for the EOS from the star's center to surface. Hereafter, we will consider  $1.4 \leq M/M_\odot \leq 1.8$  and  $10 \text{ km} \leq R \leq 14 \text{ km}$  as typical values of  $M$  and  $R$ . Such choice of  $M$  and  $R$  can duly encapsulate uncertainties of the core EOS.

Generally, a restoring force for shear torsional oscillations is provided by shear stress, which comes from the elasticity of the oscillating body and is characterized by the shear modulus  $\mu$ . In the case of torsional oscillations in the crust of a neutron star, the shear modulus is determined by the lattice energy of the Coulomb crystal that constitutes the crust. Since the crystal is generally considered to be of bcc type one can use the corresponding shear modulus, which is calculated for  $Ze$  point charges of number density  $n_i$  in the uniform neutralizing background as

$$\mu = \frac{0.1194 n_i (Ze)^2}{a}, \quad (33)$$

where  $a = (3Ze/4\pi n_e)^{1/3}$  is the radius of a Wigner-Seitz cell [66]. Note that this formula is derived in the limit of zero temperature from Monte Carlo calculations for the shear modulus averaged over all directions [67].

The shear modulus depends strongly on the value of  $L$ , which comes mainly from the  $L$  dependence of the calculated  $Z$  [10]. It is natural that one should take into account the shear modulus in pasta phases, if present, but hereafter we simply assume  $\mu = 0$  for the pasta phases. This

is because the shear modulus in the pasta phases except a phase of spherical bubbles has at least one direction in which the system is invariant with respect to translation and hence is expected to be significantly smaller than that in a phase of spherical nuclei [68]. Under this assumption, we have only to consider the shear torsional oscillations that are excited within a crustal region of spherical nuclei. Anyway, the constraint on  $L$  that will be given below can be considered to be robust, because the pasta region as shown in fig. 11 is highly limited given the resulting constraint on  $L$ .

We now consider the shear torsional oscillations on the equilibrium configuration of the crust of a neutron star described above. In order to determine the frequencies, we adopt the relativistic Cowling approximation, i.e., we neglect the metric perturbations on eq. (31) by setting  $\delta g_{\mu\nu} = 0$ . In fact, one can consider the shear torsional oscillations with satisfactory accuracy even with the relativistic Cowling approximation, because the shear torsional oscillations on a spherically symmetric star are incompressible and thus independent of the density variation during such oscillations. Additionally, due to the spherically symmetric nature of the background, we have only to consider the axisymmetric oscillations. Then, the only non-zero perturbed matter quantity is the  $\phi$  component of the perturbed four-velocity,  $\delta u^\phi$ , which can be written as

$$\delta u^\phi = e^{-\Phi} \partial_t \mathcal{Y}(t, r) \frac{1}{\sin \theta} \partial_\theta P_\ell(\cos \theta), \quad (34)$$

where  $\partial_t$  and  $\partial_\theta$  denote the partial derivatives with respect to  $t$  and  $\theta$ , respectively, while  $P_\ell(\cos \theta)$  is the  $\ell$ -th order Legendre polynomial. We remark that  $\mathcal{Y}(t, r)$  characterizes the radial dependence of the angular displacement of a matter element. By assuming that the perturbation variable  $\mathcal{Y}(t, r)$  has such a harmonic time dependence as  $\mathcal{Y}(t, r) = e^{i\omega t} \mathcal{Y}(r)$ , the perturbation equation that governs the shear torsional oscillations can be derived from the linearized equation of motion as [69]

$$\mathcal{Y}'' + \left[ \left( \frac{4}{r} + \Phi' - \Lambda' \right) + \frac{\mu'}{\mu} \right] \mathcal{Y}' + \left[ \frac{H}{\mu} \omega^2 e^{-2\Phi} - \frac{(\ell+2)(\ell-1)}{r^2} \right] e^{2\Lambda} \mathcal{Y} = 0, \quad (35)$$

where  $H$  is the enthalpy density defined as  $H \equiv \rho + p$  with the mass density  $\rho$  and pressure  $p$  as described in the previous section, and the prime denotes the derivative with respect to  $r$ . Note that under the present definition of  $H$ , effects of neutron superfluidity are essentially ignored as in ref. [64], while such effects will be included below as in ref. [65].

Once appropriate boundary conditions are imposed, the problem to solve reduces to an eigenvalue problem with respect to  $\omega$ . Since there is no matter outside the star, we adopt the zero-torque condition at the star's surface. Meanwhile, since there is no traction force in the region with  $\mu = 0$ , we adopt the zero-traction condition at the position where spherical nuclei disappear in the deepest

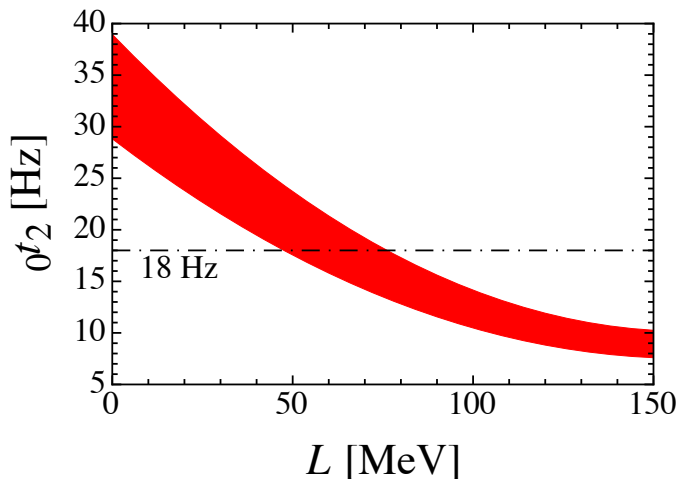


**Fig. 14.** (Color online)  ${}_0t_2$  as a function of  $L$  for  $10 \text{ km} \leq R \leq 14 \text{ km}$  and  $1.4M_\odot \leq M \leq 1.8M_\odot$ . The horizontal dot-dashed line denotes the lowest QPO frequency observed from SGR 1806-20 [62]. From ref. [64].

region of the crust. In practice, one can show that both conditions reduce to  $\mathcal{Y}' = 0$ .

For the EOS models A–I, we then calculate  ${}_0t_2$ , namely, the frequency of the mode with zero radial node and spherical harmonics  $\ell = 2$ , which is theoretically the lowest among various eigenfrequencies of the torsional oscillations. By interpolating the results for  ${}_0t_2$  and assuming  $1.4 \leq M/M_\odot \leq 1.8$  and  $10 \text{ km} \leq R \leq 14 \text{ km}$ , we obtain an allowed region as in fig. 14. We can clearly see the  $L$  dependence of the frequency, while the width comes from various sets of the star’s radius and mass. These features occur because  ${}_0t_2$  is basically determined by the ratio of the shear velocity  $\sqrt{\mu/\tilde{H}}$  over the oscillation path length through the crust. Note that the lower (upper) boundary of the allowed region in fig. 14 corresponds to the largest (smallest) and heaviest (lightest) case. In these calculations, we ignore the effects of neutron superfluidity and pasta elasticity, which act to enhance the frequency. As a result, these calculations are expected to provide a lower limit of  $L$ , hereafter referred to as  $L_{\min}$ , under the assumption that the observed QPOs in SGR giant flares arise from the torsional oscillations in neutron star crusts. In fact, since, under this assumption,  ${}_0t_2$  would be equal to or even lower than the lowest QPO frequency observed, we obtain  $L_{\min}$  of order 50 MeV, which is fairly stringent given that  $L$  is still uncertain [61]. Note that we ignore electron screening and finite-size effects on charge [70, 71], which act to reduce the shear modulus and hence  ${}_0t_2$ , as well as nuclear shell and pairing effects [72], which act to shift the nuclear charge number by keeping the local average almost unchanged. Such ignorance could modify  $L_{\min}$ .

Now, we take into account the effect of neutron superfluidity on the shear torsional oscillations [65]. In general, it is considered that neutrons confined in the nuclei start to drip therefrom when the mass density becomes higher than  $\sim 4 \times 10^{11} \text{ g cm}^{-3}$ . Then, some of the dripped neu-

trons can behave as a superfluid. A significant fraction of the dripped neutrons may move non-dissipatively with protons in the nuclei as a result of Bragg scattering off the bcc lattice of the nuclei; only neutrons in the conduction band can freely flow with respect to the lattice. In fact, the recent band calculations beyond the Wigner-Seitz approximation by Chamel [73] show that the superfluid density, which is defined here as the density of neutrons unlocked to the motion of protons in the nuclei, depends sensitively on the baryon density above neutron drip and that a considerable portion of the dripped neutrons can be locked to the motion of protons in the nuclei. On the other hand, since the shear torsional oscillations are transverse, the remaining superfluid neutrons, whose low-lying excitations are longitudinal, do not contribute to such oscillations [74].

We build the effect of neutron superfluidity into the effective enthalpy density  $\tilde{H}$ , which can be determined by subtracting the superfluid mass density from the total enthalpy density  $H$  in eq. (35) that fully contains the contributions of the superfluid neutrons as well as the nuclei and companions. Since we assume that the temperature of neutron star matter is zero, the baryon chemical potential  $\mu_b$  can be expressed as  $\mu_b = H/n_b$ . Thus, one can write down

$$\tilde{H} = \left(1 - \frac{N_s}{A}\right) H, \quad (36)$$

where  $N_s$  denotes the number of neutrons in a Wigner-Seitz cell that do not comove with protons in the nucleus, while  $A$  is the total nucleon number in the Wigner-Seitz cell. Finally, substituting  $\tilde{H}$  for  $H$  in eq. (35), one can determine the frequencies of the shear torsional oscillations, which include the effect of neutron superfluidity in a manner that depends on the value of  $N_s$ . Hereafter, we will assume that  $N_s$  comes entirely from the dripped neutron gas. Even so, it is still uncertain how much fraction of the dripped neutrons behave as a superfluid. Thus, we introduce a new parameter  $N_s/N_d$ , where  $N_d$  is the number of the dripped neutrons in the Wigner-Seitz cell. For  $N_s/N_d = 0$ , all the dripped neutrons behave as normal matter and contribute to the shear motion, while for  $N_s/N_d = 1$ , all the dripped neutrons behave as a superfluid. We remark that  $N_d - N_s$  denotes the number of the dripped neutrons bound to the nucleus. Typically, the value of  $N_s/N_d$  depends on the density inside a neutron star [73], but the case of  $N_s/N_d = 0$  in the whole crust is closer to the typical behavior than the case of  $N_s/N_d = 1$ .

We proceed to show how neutron superfluidity affects  $L_{\min}$ . For constant values of  $N_s/N_d$ , we calculate  ${}_0t_2$  by following the same line of argument as in the absence of neutron superfluidity (i.e.,  $N_s/N_d = 0$ ) and therefrom obtain  $L_{\min}$ , which is illustrated in fig. 15. One can observe that the value of  $L_{\min}$ , which is 47.6 MeV in the case of  $N_s/N_d = 0$ , can be as large as 125.9 MeV in its presence (i.e.,  $0 < N_s/N_d \leq 1$ ). In addition, we exhibit  $L_{\min} = 55.2 \text{ MeV}$ , the result from the realistic band calculations of  $N_s/N_d$  in ref. [73]. This  $L_{\min}$  is expected to give a reliable constraint on  $L$ , although a possible  $L$  dependence of  $N_s/N_d$  through the band structure remains to be investigated.

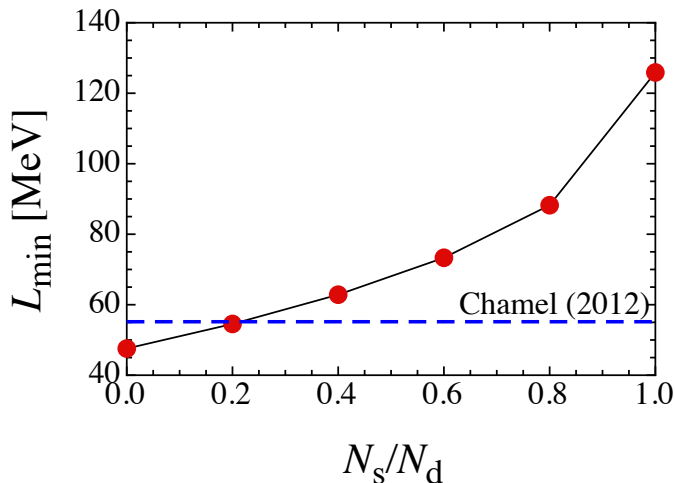


**Fig. 15.** (Color online)  $L_{\min}$  as a function of  $N_s/N_d$ , the fraction of superfluid neutrons. The horizontal broken line corresponds to the result from the band calculations of  $N_s/N_d$  by Chamel [73]. From ref. [65].

Instead of just considering  $L_{\min}$ , we can obtain a more stringent constraint on  $L$  by fitting the predicted frequencies of fundamental torsional oscillations with different values of  $\ell$  to the low-lying QPO frequencies observed in SGRs. To this end, we use the values of  $N_s/N_d$  derived by Chamel [73]. In the present analysis, we focus on the observed QPO frequencies lower than 100 Hz, i.e., 18, 26, 30, and 92.5 Hz in SGR 1806-20 and 28, 54, and 84 Hz in SGR 1900+14 [62]. In fact, the even higher observed frequencies would be easier to explain in terms of multipolar fundamental and overtone frequencies. Because of the small interval between the observed frequencies 26 and 30 Hz in SGR 1806-20, it is more difficult to explain the QPO frequencies observed in SGR 1806-20 than those in SGR 1900+14. If one identifies the lowest frequency in SGR 1806-20 (18 Hz) as the fundamental torsional oscillation with  $\ell = 3$ , one can reasonably explain 26, 30, and 92.5 Hz in terms of those with  $\ell = 4, 5$ , and 15. In the case of the typical neutron star model with  $M = 1.4M_{\odot}$  and  $R = 12$  km, we compare the predicted frequencies with the observed ones as shown in fig. 16. One can observe from this figure that the best value of  $L$  to reproduce the observed frequencies is  $L = 127.1$  MeV, where the calculated frequencies, 18.5 Hz ( $\ell = 3$ ), 24.9 Hz ( $\ell = 4$ ), 31.0 Hz ( $\ell = 5$ ), and 90.3 Hz ( $\ell = 15$ ), are within less than 5% deviations from the observations.

Let us now extend the analysis to different stellar models and to SGR 1900+14. We find that the QPOs observed in SGR 1806-20 can be explained in terms of the eigenfrequencies of the same  $\ell$  within similar deviations even for different stellar models except for the case with  $M = 1.4M_{\odot}$  and  $R = 10$  km, while the low-lying QPOs observed in SGR 1900+14 can be similarly explained in terms of the fundamental torsional oscillations with  $\ell = 4, 8$ , and 13. As a result, the allowed region of  $L$  where the QPO frequencies observed in SGR 1806-20 and in SGR 1900+14 are reproducible simultaneously lies in the range

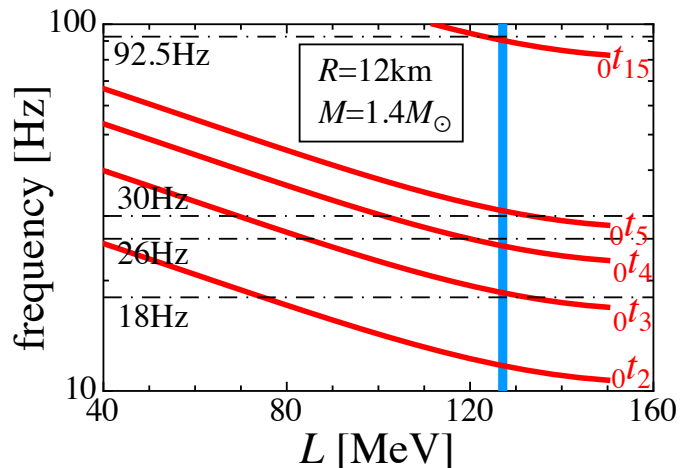


**Fig. 16.** (Color online) Comparison of the calculated frequencies of torsional oscillations (solid lines) with the QPO frequencies observed in SGR 1806-20 (dot-dashed lines), where the stellar model adopted in the calculations is  $M/M_{\odot} = 1.4$  and  $R = 12$  km. The vertical line corresponds to the value of  $L$  that is consistent with the observations. From ref. [65].

$101.0 \text{ MeV} \leq L \leq 130.1 \text{ MeV}$ , as long as the oscillating neutron stars have mass and radius ranging  $1.4 \leq M/M_{\odot} \leq 1.8$  and  $10 \text{ km} \leq R \leq 14 \text{ km}$ . It is interesting to compare this constraint with various experimental constraints on  $L$  [61], which have yet to converge but seemingly favor smaller  $L$ . Note that if we extend the mass range to, e.g.,  $1.0 \leq M/M_{\odot} \leq 1.8$ , this constraint would be broader with the lower bound unchanged, while the values of  $L_{\min}$  in fig. 15 would be unchanged. This is because of larger  ${}_{0t_2}$  for smaller  $M$ .

In principle, there are many other ways of identifying the observed QPOs. For example, magnetic oscillations and magneto-elastic oscillations [75,76] have been already invoked as such candidates. Our analyses, however, imply that as good a reproduction of the observed low-lying frequencies as shown in fig. 16 would be desired. It is an open issue to ask if there could be a new way of reasonable identification that predicts a lower  $L$ .

## 8 Epilogue

As we have shown by using the macroscopic nuclear model, the parameter  $L$  controlling the density dependence of the symmetry energy is closely related to the size and mass of unstable nuclei in laboratories and to the pasta region and shear modes in neutron star crusts. Ongoing and future developments of neutron star observatories and RI beam facilities are thus expected to help determining  $L$  sufficiently well. For such determination, systematic errors involved in connecting  $L$  with observables would have to be duly taken into account, no matter whether the macroscopic nuclear model is used or not.

## Acknowledgments

We are indebted to our collaborators of the works underlying the present contribution, namely, B. Abu-Ibrahim, A. Kohama, H. Koura, K. Nakazato, and H. Sotani. This work was supported in part by Grants-in-Aid for Scientific Research on Innovative Areas through No. 24105008 provided by MEXT.

## References

1. H. Heiselberg, V.R. Pandharipande, *Annu. Rev. Nucl. Part. Sci.* **50**, 481 (2000).
2. T. Krüger, I. Tews, K. Hebeler, A. Schwenk, *Phys. Rev. C* **88**, 025802 (2013).
3. J.M. Lattimer, *Annu. Rev. Nucl. Part. Sci.* **31**, 337 (1981).
4. J. Carlson, J. Morales, V.R. Pandharipande, D.G. Ravenhall, *Phys. Rev. C* **68**, 025802 (2003).
5. B. Friedman, V.R. Pandharipande, *Nucl. Phys. A* **361**, 502 (1981).
6. K. Oyamatsu, K. Iida, *Prog. Theor. Phys.* **109**, 631 (2003).
7. J.M. Lattimer, M. Prakash, *Science* **304**, 536 (2004).
8. K. Oyamatsu, *Nucl. Phys. A* **561**, 431 (1993).
9. I.E. Lagaris, V.R. Pandharipande, *Nucl. Phys. A* **369**, 470 (1981).
10. K. Oyamatsu, K. Iida, *Phys. Rev. C* **75**, 015801 (2007).
11. A.R. Bodmer, Q.N. Usmani, *Phys. Rev. C* **67**, 034305 (2003).
12. L.R.B. Elton, A. Swift, *Nucl. Phys. A* **94**, 52 (1967).
13. G. Audi, A.H. Wapstra, *Nucl. Phys. A* **595**, 409 (1995).
14. H. de Vries, C.W. de Jager, C. de Vries, *At. Data Nucl. Data Tables* **36**, 495 (1987).
15. A. Ozawa *et al.*, *Phys. Lett. B* **334**, 18 (1994).
16. L. Chulkov *et al.*, *Nucl. Phys. A* **603**, 219 (1996).
17. A. Ozawa *et al.*, *Nucl. Phys. A* **709**, 60 (2002).
18. M. Farine, J.M. Pearson, B. Rouben, *Nucl. Phys. A* **304**, 317 (1978).
19. S. Gandolfi, J. Carlson, S. Reddy, *Phys. Rev. C* **85**, 032801(R) (2012).
20. M. Kortelainen, T. Lesinski, J. Moré, W. Nazarewicz, J. Sarich, N. Schunck, M.V. Stoitsov, S. Wild, *Phys. Rev. C* **82**, 024313 (2010).
21. M.B. Tsang *et al.*, *Phys. Rev. C* **86**, 015803 (2012).
22. J.P. Blaizot, *Phys. Rep.* **64**, 171 (1980).
23. J.B. Natowitz, K. Hagel, Y. Ma, M. Murray, L. Qin, R. Wada, J. Wang, *Phys. Rev. Lett.* **89**, 212701 (2002).
24. E. Khan, J. Margueron, arXiv:1304.4721.
25. A. Kohama, K. Iida, K. Oyamatsu, *Phys. Rev. C* **69**, 064316 (2004).
26. C.J. Batty, E. Friedman, H.J. Gils, H. Rebel, *Adv. Nucl. Phys.* **19**, 1 (1989).
27. X. Roca-Maza, M. Centelles, X. Viñas, M. Warda, *Phys. Rev. Lett.* **106**, 252501 (2011).
28. M. Yamada, *Prog. Theor. Phys.* **32**, 512 (1964).
29. K. Iida, K. Oyamatsu, *Phys. Rev. C* **69**, 037301 (2004).
30. L. Ray, G.W. Hoffmann, W.R. Coker, *Phys. Rep.* **212**, 223 (1992).
31. R.J. Glauber, in *Lectures in theoretical physics*, eds. W.E. Brittin, L.C. Dunham (Interscience, New York, 1959), Vol. 1, p. 315.
32. K. Iida, K. Oyamatsu, B. Abu-Ibrahim, *Phys. Lett. B* **576**, 273 (2003).
33. I. Ahmad, *Nucl. Phys. A* **247**, 418 (1975).
34. L. Ray, *Phys. Rev. C* **20**, 1857 (1979).
35. L. Ray, W.R. Coker, G.W. Hoffmann, *Phys. Rev. C* **18**, 2641 (1978).
36. K. Iida, K. Oyamatsu, B. Abu-Ibrahim, A. Kohama, *Prog. Theor. Phys.* **126**, 1091 (2011).
37. A. Ingemarsson, M. Lantz, *Phys. Rev. C* **72**, 064615 (2005).
38. K. Iida, A. Kohama, K. Oyamatsu, *J. Phys. Soc. Japan* **76**, 044201 (2007).
39. A. Kohama, K. Iida, K. Oyamatsu, *Phys. Rev. C* **78**, 061601(R) (2008).
40. I.S. Novikov, Y. Shabelski, arXiv:1302.3930.
41. K. Oyamatsu, K. Iida, *Phys. Rev. C* **81**, 054302 (2010).
42. K. Oyamatsu, K. Iida, H. Koura, *Phys. Rev. C* **82**, 027301 (2010).
43. H. Koura, T. Tachibana, M. Uno, M. Yamada, *Prog. Theor. Phys.* **113**, 305 (2005).
44. *Chart of the Nuclides 2004*, compiled by T. Horiguchi *et al.*, JNDC and Nuclear Data Center, JAERI (2005).
45. G. Audi, A.H. Wapstra, C. Thibault, *Nucl. Phys. A* **729**, 337 (2003).
46. M. Notani *et al.*, *Phys. Rev. C* **76**, 044605 (2007).
47. T. Baumann *et al.*, *Nature (London)* **449**, 1022 (2007).
48. C.J. Pethick, D.G. Ravenhall, *Annu. Rev. Nucl. Part. Sci.* **45**, 429 (1995).
49. N. Chamel, P. Haensel, *Living Rev. Relativity* **11**, 10 (2008).
50. K. Oyamatsu, M. Hashimoto, M. Yamada, *Prog. Theor. Phys.* **72**, 373 (1984).
51. T. Maruyama, G. Watanabe, S. Chiba, *Prog. Theor. Exp. Phys.* **1**, 01A201 (2012).
52. W.G. Newton, J.R. Stone, *Phys. Rev. C* **79**, 055801 (2009).
53. H. Pais, J.R. Stone, *Phys. Rev. Lett.* **109**, 151101 (2012).
54. F. Sébille, S. Figerou, V. de la Mota, *Nucl. Phys. A* **822**, 51 (2009).
55. F. Sébille, V. de la Mota, S. Figerou, *Phys. Rev. C* **84**, 055801 (2011).
56. B. Schuetrumpf, M.A. Klatt, K. Iida, J.A. Maruhn, K. Mecke, P.-G. Reinhard, *Phys. Rev. C* **87**, 055805 (2013).
57. K. Nakazato, K. Oyamatsu, S. Yamada, *Phys. Rev. Lett.* **103**, 132501 (2009).
58. K. Nakazato, K. Iida, K. Oyamatsu, *Phys. Rev. C* **83**, 065811 (2011).
59. F.S. Bates, G.H. Fredrickson, *Phys. Today* **52**, No. 2, 32 (1999).
60. G. Watanabe, K. Iida, K. Sato, *Nucl. Phys. A* **676**, 455 (2000); Erratum, *ibid.* **726**, 357 (2003).
61. W.G. Newton, M. Gearheart, D.H. Wen, B.A. Li, *J. Phys.: Conf. Ser.* **420**, 012145 (2013).
62. A.L. Watts, T.E. Strohmayer, *Adv. Space Res.* **40**, 1446 (2006).
63. A.W. Steiner, A.L. Watts, *Phys. Rev. Lett.* **103**, 181101 (2009).
64. H. Sotani, K. Nakazato, K. Iida, K. Oyamatsu, *Phys. Rev. Lett.* **108**, 201101 (2012).
65. H. Sotani, K. Nakazato, K. Iida, K. Oyamatsu, *Mon. Not. R. Astron. Soc.* **428**, L21 (2013).
66. T. Strohmayer, H.M. van Horn, S. Ogata, H. Iyetomi, S. Ichimaru, *Astrophys. J.* **375**, 679 (1991).
67. S. Ogata, S. Ichimaru, *Phys. Rev. A* **42**, 4867 (1990).
68. C.J. Pethick, A.Y. Potekhin, *Phys. Lett. B* **427**, 7 (1998).



69. B.L. Schumaker, K.S. Thorne, 1983, *Mon. Not. R. Astron. Soc.* **203**, 457 (1983).
70. G. Baym, H.A. Bethe, C.J. Pethick, *Nucl. Phys. A* **175**, 225 (1971).
71. C.J. Horowitz, J. Hughto, arXiv:0812.2650.
72. A.T. Deibel, A.W. Steiner, E.F. Brown, arXiv:1303.3270.
73. N. Chamel, *Phys. Rev. C* **85**, 035801 (2012).
74. C.J. Pethick, N. Chamel, S. Reddy, *Prog. Theor. Phys. Suppl.* **186**, 9 (2010).
75. A. Passamonti, S.K. Lander, *Mon. Not. R. Astron. Soc.* **429**, 767 (2013).
76. M. Gabler, P. Cerdá-Durán, N. Stergioulas, J.A. Font, E. Müller, arXiv:1304.3566.